

Supplemental Material for “Sublattice-sensitive Majorana modes”

Di Zhu,^{1,*} Bo-Xuan Li,^{2,3,*} and Zhongbo Yan^{1,†}

¹*School of Physics, Sun Yat-Sen University, Guangzhou 510275, China*

²*Beijing National Laboratory for Condensed Matter Physics and Institute of Physics, Chinese Academy of Sciences, Beijing 100190, China*

³*University of Chinese Academy of Sciences, Beijing 100049, China*

(Dated: November 8, 2022)

This supplemental material contains six sections, including: (I) the derivation of low-energy boundary Hamiltonians for beard and zigzag edges; (II) two-dimensional honeycomb-lattice topological insulators in proximity to d-wave superconductors; (III) the impact of finite chemical potential on the topological criterion; (IV) sublattice-sensitive Majorana modes in time-reversal symmetry broken systems; (V) manipulating the positions of Majorana zero modes by electrically controlling the local boundary potential; (VI) Sublattice-sensitive Majorana Kramers pairs in Lieb lattices.

I. THE DERIVATION OF LOW-ENERGY BOUNDARY HAMILTONIANS FOR BEARD AND ZIGZAG EDGES

We start with the real-space Hamiltonian,

$$\begin{aligned}
 H = & t \sum_{\langle ij \rangle, \alpha} c_{i, \alpha}^\dagger c_{j, \alpha} + i \lambda_{so} \sum_{\langle \langle ij \rangle \rangle, \alpha, \beta} \nu_{ij} c_{i, \alpha}^\dagger (s^z)_{\alpha \beta} c_{j, \beta} \\
 & - \mu \sum_{i, \alpha} c_{i, \alpha}^\dagger c_{i, \alpha} + [\Delta_0 \sum_i c_{i, \uparrow}^\dagger c_{i, \downarrow}^\dagger + \sum_{\langle ij \rangle} \Delta_{1; ij} c_{i, \uparrow}^\dagger c_{j, \downarrow}^\dagger \\
 & + \sum_{\langle \langle ij \rangle \rangle} \Delta_{2; ij} c_{i, \uparrow}^\dagger c_{j, \downarrow}^\dagger + h.c.], \tag{S1}
 \end{aligned}$$

where t , λ_{so} and μ denote the nearest-neighbor hopping constant, spin-orbit coupling coefficient, and chemical potential, respectively. Δ_0 , $\Delta_{1; ij}$ and $\Delta_{2; ij}$ denote the on-site, nearest-neighbor and next-nearest-neighboring pairing, respectively.

To derive the low-energy boundary Hamiltonian, we need to first perform a Fourier transformation to obtain the Bogoliubov-de Gennes (BdG) Hamiltonian in momentum space. The Fourier transformation is given by

$$c_{j \in A(B), \alpha} = \frac{1}{\sqrt{N}} \sum_{j \in A(B)} c_{A(B), \mathbf{k}, \alpha} e^{i \mathbf{k} \cdot (\mathbf{r}_j + \boldsymbol{\delta}_{A(B)})}, \quad c_{j \in A(B), \alpha}^\dagger = \frac{1}{\sqrt{N}} \sum_{j \in A(B)} c_{A(B), \mathbf{k}, \alpha}^\dagger e^{-i \mathbf{k} \cdot (\mathbf{r}_j + \boldsymbol{\delta}_{A(B)})} \tag{S2}$$

where N denotes the number of unit cells, \mathbf{r}_j labels the coordinate of the j th unit cell, and $\boldsymbol{\delta}_{A(B)}$ describes the locations of $A(B)$ sublattice in the unit cell. Choosing the Nambu basis as $\Psi_{\mathbf{k}} = (c_{A, \mathbf{k}, \uparrow}, c_{B, \mathbf{k}, \uparrow}, c_{A, \mathbf{k}, \downarrow}, c_{B, \mathbf{k}, \downarrow}, c_{A, -\mathbf{k}, \uparrow}^\dagger, c_{B, -\mathbf{k}, \uparrow}^\dagger, c_{A, -\mathbf{k}, \downarrow}^\dagger, c_{B, -\mathbf{k}, \downarrow}^\dagger)^T$, the BdG Hamiltonian reads

$$\begin{aligned}
 \mathcal{H}_{\text{BdG}}(\mathbf{k}) = & t(2 \cos \frac{\sqrt{3}k_x}{2} \cos \frac{k_y}{2} + \cos k_y) \tau_z s_0 \sigma_x - t(2 \cos \frac{\sqrt{3}k_x}{2} \sin \frac{k_y}{2} - \sin k_y) \tau_z s_0 \sigma_y \\
 & + 2 \lambda_{so} (\sin \sqrt{3}k_x - 2 \sin \frac{\sqrt{3}k_x}{2} \cos \frac{3k_y}{2}) \tau_0 s_z \sigma_z - \mu \tau_z s_0 \sigma_0 \\
 & - \Delta_1 (2 \cos \frac{\sqrt{3}k_x}{2} \cos \frac{k_y}{2} + \cos k_y) \tau_y s_y \sigma_x + \Delta_1 (2 \cos \frac{\sqrt{3}k_x}{2} \sin \frac{k_y}{2} - \sin k_y) \tau_y s_y \sigma_y \\
 & - [\Delta_0 + 2 \Delta_2 (\cos \sqrt{3}k_x + 2 \cos \frac{\sqrt{3}k_x}{2} \cos \frac{3k_y}{2})] \tau_y s_y \sigma_0. \tag{S3}
 \end{aligned}$$

For notational simplicity, we have set the lattice constant to unity. For the convenience of discussion, throughout this work, t and λ_{so} will be assumed to be positive. As we have shown numerically that the nearest-neighbor pairing has a negligible effect to the helical edge states, below we also set $\Delta_1 = 0$ for simplicity.

According to numerical calculations, we know that for a cylindrical geometry with periodic boundary condition in the x direction and open boundary condition in the y direction, the boundary Dirac point, which corresponds to the crossing point of the energy spectrum of the normal-state helical edge states, is located at $k_x = 0$ ($k_x = \pi/\sqrt{3}$) for a beard (zigzag) edge. Below let us focus on the upper y -normal boundary and derive the corresponding low-energy boundary Hamiltonians for both beard and zigzag edges.

I. A. Low-energy boundary Hamiltonian for the beard edge

When the upper boundary is a beard edge, the terminating sublattices are type A. As numerical calculations reveal that the boundary Dirac point for such an edge will appear at $k_x = 0$, in order to derive the low-energy boundary Hamiltonian, we perform an expansion of the bulk Hamiltonian around $k_x = 0$ up to the linear order in momentum. Accordingly, the Hamiltonian becomes

$$\begin{aligned}\mathcal{H}_{\text{BdG}}(q_x, k_y) = & t(2 \cos \frac{k_y}{2} + \cos k_y) \tau_z s_0 \sigma_x - t(2 \sin \frac{k_y}{2} - \sin k_y) \tau_z s_0 \sigma_y \\ & + 2\sqrt{3} \lambda_{so} q_x (1 - \cos \frac{3k_y}{2}) \tau_0 s_z \sigma_z - \mu \tau_z s_0 \sigma_0 \\ & - [\Delta_0 + 2\Delta_2 (1 + 2 \cos \frac{3k_y}{2})] \tau_y s_y \sigma_0,\end{aligned}\quad (\text{S4})$$

where q_x denotes a small momentum measured from $k_x = 0$. Next, we decompose the Hamiltonian into two parts, $\mathcal{H}_{\text{BdG}} = \mathcal{H}_1 + \mathcal{H}_2$, with

$$\begin{aligned}\mathcal{H}_1(q_x, k_y) = & t(2 \cos \frac{k_y}{2} + \cos k_y) \tau_z s_0 \sigma_x - t(2 \sin \frac{k_y}{2} - \sin k_y) \tau_z s_0 \sigma_y, \\ \mathcal{H}_2(q_x, k_y) = & 2\sqrt{3} \lambda_{so} q_x (1 - \cos \frac{3k_y}{2}) \tau_0 s_z \sigma_z - \mu \tau_z s_0 \sigma_0 - [\Delta_0 + 2\Delta_2 (1 + 2 \cos \frac{3k_y}{2})] \tau_y s_y \sigma_0.\end{aligned}\quad (\text{S5})$$

For real materials, $\lambda_{so} \ll t$ and $\Delta_i \ll t$ are naturally satisfied. As we are interested in the regime where q_x is small, the whole \mathcal{H}_2 can be treated as a perturbation if the chemical potential is also assumed to be close to the neutrality condition.

In the following, let us consider a half-infinity sample with the boundary corresponding to the upper beard edge. In the basis $\Psi_{q_x} = (c_{1,A,q_x}, c_{1,B,q_x}, c_{2,A,q_x}, c_{2,B,q_x}, \dots, c_{n,A,q_x}, c_{n,B,q_x}, \dots)^T$ with $c_{n,A(B),q_x} = (c_{n,A(B),q_x,\uparrow}, c_{n,A(B),q_x,\downarrow}, c_{n,A(B),-q_x,\uparrow}^\dagger, c_{n,A(B),-q_x,\downarrow}^\dagger)$, the Hamiltonian in the matrix form reads

$$\mathcal{H}_1 = \begin{pmatrix} 0 & t\tau_z s_0 & 0 & 0 & 0 & 0 & \dots \\ t\tau_z s_0 & 0 & 2t\tau_z s_0 & 0 & 0 & 0 & \dots \\ 0 & 2t\tau_z s_0 & 0 & t\tau_z s_0 & 0 & 0 & \dots \\ 0 & 0 & t\tau_z s_0 & 0 & 2t\tau_z s_0 & 0 & \dots \\ 0 & 0 & 0 & 2t\tau_z s_0 & 0 & t\tau_z s_0 & \dots \\ 0 & 0 & 0 & 0 & t\tau_z s_0 & 0 & \dots \\ \vdots & \vdots & \vdots & \vdots & \vdots & \vdots & \ddots \end{pmatrix}. \quad (\text{S6})$$

To see that this Hamiltonian has solutions for zero-energy bound states, we solve the eigenvalue equation $\mathcal{H}_1 |\Psi_\alpha\rangle = 0$. Concretely, as τ_z and s_z both commute with \mathcal{H}_1 , the eigenvector $|\Psi_\alpha\rangle$ can be assigned with the form

$$|\Psi_{\tau s}\rangle = |\tau_z = \tau\rangle \otimes |s_z = s\rangle \otimes (\psi_{1A}, \psi_{1B}, \psi_{2A}, \psi_{2B}, \dots, \psi_{nA}, \psi_{nB}, \dots)^T, \quad (\text{S7})$$

where $\tau = \pm 1$ and $s = \pm 1$ correspond to the two possible eigenvalues of τ_z and s_z , respectively. Taking the expression of $|\Psi_{\tau s}\rangle$ back into the eigenvalue equation $\mathcal{H}_1 |\Psi_{\tau s}\rangle = 0$, one gets a series of equations with periodic structures, which read

$$\begin{aligned}t_\tau \psi_{1B} &= 0, \\ t_\tau \psi_{1A} + 2t_\tau \psi_{2A} &= 0, \\ 2t_\tau \psi_{1B} + t_\tau \psi_{2B} &= 0, \\ &\dots \\ t_\tau \psi_{nA} + 2t_\tau \psi_{(n+1)A} &= 0, \\ 2t_\tau \psi_{nB} + t_\tau \psi_{(n+1)B} &= 0, \\ &\dots,\end{aligned}\quad (\text{S8})$$

where $t_\tau \equiv t\tau$. According to the periodic structures, one can easily find

$$\psi_{(n+1)A} = -\frac{1}{2} \psi_{nA}, \quad \psi_{nB} = 0. \quad (\text{S9})$$

Therefore, the eigenvectors take the form

$$|\Psi_{\tau s}\rangle = |\tau_z = \tau\rangle \otimes |s_z = s\rangle \otimes \mathcal{N}(1, 0, -\frac{1}{2}, 0, \dots, (-\frac{1}{2})^{(n-1)}, 0, \dots)^T, \quad (\text{S10})$$

where the normalization constant \mathcal{N} is determined by the normalization condition $\langle \Psi_{\tau s} | \Psi_{\tau s} \rangle = 1$. Simple algebra calculations give

$$\mathcal{N}^2 \sum_{n=0}^{\infty} \frac{1}{2^{2n}} = \mathcal{N}^2 \frac{1}{1 - \frac{1}{4}} = \frac{4}{3} \mathcal{N}^2 = 1, \quad (\text{S11})$$

indicating $\mathcal{N} = \frac{\sqrt{3}}{2}$. As ψ_{nA} decays in a power law with the increase of n , the existence of four such eigenvectors indicates the existence of four zero-energy bound states. It is worth noting that the topological insulator has one pair of helical states on a given edge, but the introduce of particle-hole degrees of freedom doubles the number of helical states. Next, we project \mathcal{H}_2 onto the basis spanned by the four zero-energy eigenvectors. To proceed, we write down the matrix form for each term in \mathcal{H}_2 .

Let us first focus on the term $\mathcal{H}_{2,1} = 2\sqrt{3}\lambda_{so}q_x(1 - \cos \frac{3k_y}{2})\tau_0 s_z \sigma_z$. In the basis $\Psi_{q_x} = (c_{1,A,q_x}, c_{1,B,q_x}, c_{2,A,q_x}, c_{2,B,q_x}, \dots, c_{n,A,q_x}, c_{n,B,q_x}, \dots)^T$, its matrix form is

$$\mathcal{H}_{2,1} = \tau_0 \otimes s_z \otimes \begin{pmatrix} 2\sqrt{3}\lambda_{so}q_x & 0 & -\sqrt{3}\lambda_{so}q_x & 0 & 0 & 0 & \dots \\ 0 & -2\sqrt{3}\lambda_{so}q_x & 0 & \sqrt{3}\lambda_{so}q_x & 0 & 0 & \dots \\ -\sqrt{3}\lambda_{so}q_x & 0 & 2\sqrt{3}\lambda_{so}q_x & 0 & -\sqrt{3}\lambda_{so}q_x & 0 & \dots \\ 0 & \sqrt{3}\lambda_{so}q_x & 0 & -2\sqrt{3}\lambda_{so}q_x & 0 & \sqrt{3}\lambda_{so}q_x & \dots \\ 0 & 0 & -\sqrt{3}\lambda_{so}q_x & 0 & 2\sqrt{3}\lambda_{so}q_x & 0 & \dots \\ 0 & 0 & 0 & \sqrt{3}\lambda_{so}q_x & 0 & -2\sqrt{3}\lambda_{so}q_x & \dots \\ \vdots & \vdots & \vdots & \vdots & \vdots & \vdots & \ddots \end{pmatrix}. \quad (\text{S12})$$

Then the contribution from $\mathcal{H}_{2,1}$ to the boundary Hamiltonian is

$$\begin{aligned} (\mathcal{H}_{beard,1})_{\tau s, \tau' s'} &= \langle \Psi_{\tau s} | \mathcal{H}_{2,1} | \Psi_{\tau' s'} \rangle \\ &= 2\sqrt{3}\lambda_{so,s}q_x \delta_{\tau\tau'} \delta_{ss'} - \sqrt{3}\lambda_{so,s}q_x \delta_{\tau\tau'} \delta_{ss'} \mathcal{N}^2 \sum_{n=1}^{+\infty} 2\psi_{nA} \psi_{(n+1)A} \\ &= 2\sqrt{3}\lambda_{so,s}q_x \delta_{\tau\tau'} \delta_{ss'} + \sqrt{3}\lambda_{so,s}q_x \delta_{\tau\tau'} \delta_{ss'} \mathcal{N}^2 \sum_{n=1}^{+\infty} \psi_{nA} \psi_{nA} \\ &= 2\sqrt{3}\lambda_{so,s}q_x \delta_{\tau\tau'} \delta_{ss'} + \sqrt{3}\lambda_{so,s}q_x \delta_{\tau\tau'} \delta_{ss'} \\ &= 3\sqrt{3}\lambda_{so,s}q_x \delta_{\tau\tau'} \delta_{ss'}, \end{aligned} \quad (\text{S13})$$

where $\lambda_{so,s} \equiv \lambda_{so}s$. In the derivation above, a few facts have been used, including: (1) ψ_{nA} is real; (2) $\psi_{(n+1)A} = -\frac{1}{2}\psi_{nA}$; (3) $\mathcal{N}^2 \sum_{n=1}^{+\infty} \psi_{nA}^2 = 1$. Choosing the basis spanning the subspace for boundary Hamiltonian to be $(|\Psi_{11}\rangle, |\Psi_{1-1}\rangle, |\Psi_{-11}\rangle, |\Psi_{-1-1}\rangle)^T$, $\mathcal{H}_{beard,1}$ can be expressed in terms of the Pauli matrices as

$$\mathcal{H}_{beard,1} = 3\sqrt{3}\lambda_{so}q_x \tau_0 s_z. \quad (\text{S14})$$

For the second term $\mathcal{H}_{2,2} = -\mu\tau_z s_0 \sigma_0$, as it is diagonal in the basis Ψ_{q_x} , one can easily find that its contribution to the boundary Hamiltonian is just

$$\mathcal{H}_{beard,2} = -\mu\tau_z s_0. \quad (\text{S15})$$

Now let us analyze the contribution from the pairing term. In the basis Ψ_{q_x} , the matrix form of the pairing term is

$$\mathcal{H}_{2,3} = - \begin{pmatrix} (\Delta_0 + 2\Delta_2)\tau_y s_y & 0 & 2\Delta_2\tau_y s_y & 0 & \dots \\ 0 & (\Delta_0 + 2\Delta_2)\tau_y s_y & 0 & 2\Delta_2\tau_y s_y & \dots \\ 2\Delta_2\tau_y s_y & 0 & (\Delta_0 + 2\Delta_2)\tau_y s_y & 0 & \dots \\ 0 & 2\Delta_2\tau_y s_y & 0 & (\Delta_0 + 2\Delta_2)\tau_y s_y & \dots \\ \vdots & \vdots & \vdots & \vdots & \ddots \end{pmatrix}. \quad (\text{S16})$$

Similarly, its contribution to the boundary Hamiltonian is

$$\begin{aligned}
(\mathcal{H}_{beard,3})_{\tau s, \tau' s'} &= \langle \Psi_{\tau s} | \mathcal{H}_{2,3} | \Psi_{\tau' s'} \rangle \\
&= -(\Delta_0 + 2\Delta_2)(\tau_y)_{\tau\tau'}(s_y)_{ss'} - 2\Delta_2(\tau_y)_{\tau\tau'}(s_y)_{ss'} \mathcal{N}^2 \sum_{n=1}^{+\infty} 2\psi_{nA}\psi_{(n+1)A} \\
&= -(\Delta_0 + 2\Delta_2)(\tau_y)_{\tau\tau'}(s_y)_{ss'} + 2\Delta_2(\tau_y)_{\tau\tau'}(s_y)_{ss'} \\
&= -\Delta_0(\tau_y)_{\tau\tau'}(s_y)_{ss'}.
\end{aligned} \tag{S17}$$

One finds that the contribution from the next-nearest-neighbor pairing will vanish for the beard edge, in agreement with the numerical results shown in Fig.2 of the main text. In terms of the Pauli matrices, its form is just

$$\mathcal{H}_{beard,3} = -\Delta_0 \tau_y s_y. \tag{S18}$$

Taking all contributions together, we reach the final expression of the boundary Hamiltonian for the upper beard edge, which reads

$$\mathcal{H}_{beard} = \mathcal{H}_{b,1} + \mathcal{H}_{b,2} + \mathcal{H}_{b,3} = vq_x \tau_0 s_z - \mu \tau_z s_0 - \Delta_0 \tau_y s_y, \tag{S19}$$

where $v = 3\sqrt{3}\lambda_{so}$. In the limit $\mu = 0$, the boundary Hamiltonian reduces to the form of Eq.(8) in the main text. We find that the boundary energy gap at $k_x = 0$ predicted by the low-energy boundary Hamiltonian agree perfectly with the numerical results when only the on-site pairing or the next-nearest-neighbor pairing is present. When both the on-site and the next-nearest-neighbor pairings are finite, the boundary energy gap is found to be a little smaller than the predicted value $E_g = 2|\Delta_0|$, but the agreement is still very good at the neighborhood of the boundary Dirac point.

I. B. Low-energy boundary Hamiltonian for the zigzag edge

When the upper edge changes to be terminated at type-B sublattices, so a zigzag edge, numerical results show that the boundary Dirac point is shifted to $k_x = \pi/\sqrt{3}$. In order to analytically derive the corresponding boundary Hamiltonian, we similarly perform an expansion around $k_x = \pi/\sqrt{3}$ and keep the momentum up to the linear order. Accordingly, the Hamiltonian becomes

$$\begin{aligned}
\mathcal{H}_{\text{BdG}}(q'_x, k_y) &= t(-\sqrt{3}q'_x \cos \frac{k_y}{2} + \cos k_y) \tau_z s_0 \sigma_x + t(\sqrt{3}q'_x \sin \frac{k_y}{2} + \sin k_y) \tau_z s_0 \sigma_y \\
&\quad + 2\lambda_{so}(-\sqrt{3}q'_x - 2 \cos \frac{3k_y}{2}) \tau_0 s_z \sigma_z - \mu \tau_z s_0 \sigma_0 \\
&\quad - [\Delta_0 + 2\Delta_2(-1 - \sqrt{3}q'_x \cos \frac{3k_y}{2})] \tau_y s_y \sigma_0,
\end{aligned} \tag{S20}$$

where q'_x denotes a small momentum measured from $k_x = \pi/\sqrt{3}$. Similar to the previous case, we decompose the Hamiltonian into two parts, $\mathcal{H} = \mathcal{H}_1 + \mathcal{H}_2$, with

$$\begin{aligned}
\mathcal{H}_1(q'_x, k_y) &= t \cos k_y \tau_z s_0 \sigma_x + t \sin k_y \tau_z s_0 \sigma_y - 4\lambda_{so} \cos \frac{3k_y}{2} \tau_0 s_z \sigma_z, \\
\mathcal{H}_2(q'_x, k_y) &= -\sqrt{3}tq'_x \cos \frac{k_y}{2} \tau_z s_0 \sigma_x + \sqrt{3}tq'_x \sin \frac{k_y}{2} \tau_z s_0 \sigma_y \\
&\quad - 2\sqrt{3}\lambda_{so}q'_x \tau_0 s_z \sigma_z - \mu \tau_z s_0 \sigma_0 \\
&\quad - [\Delta_0 + 2\Delta_2(-1 - \sqrt{3}q'_x \cos \frac{3k_y}{2})] \tau_y s_y \sigma_0.
\end{aligned} \tag{S21}$$

As we are interested in the small q'_x regime, it is also justified to treat the whole \mathcal{H}_2 as a perturbation.

When the upper edge becomes a zigzag one, the terminating sublattices become type B, so the corresponding basis for a half-infinity system becomes $\Psi_{q'_x} = (c_{1,B,q'_x}, c_{2,A,q'_x}, c_{2,B,q'_x}, c_{3,A,q'_x}, c_{3,B,q'_x}, \dots, c_{n,A,q'_x}, c_{n,B,q'_x}, \dots)^T$. Then \mathcal{H}_1 in matrix form

reads

$$\mathcal{H}_1 = \begin{pmatrix} 0 & 0 & 2\lambda_{so}\tau_0 s_z & 0 & 0 & 0 & \cdots \\ 0 & 0 & t\tau_z s_0 & -2\lambda_{so}\tau_0 s_z & 0 & 0 & \cdots \\ 2\lambda_{so}\tau_0 s_z & t\tau_z s_0 & 0 & 0 & 2\lambda_{so}\tau_0 s_z & 0 & \cdots \\ 0 & -2\lambda_{so}\tau_0 s_z & 0 & 0 & t\tau_z s_0 & -2\lambda_{so}\tau_0 s_z & \cdots \\ 0 & 0 & 2\lambda_{so}\tau_0 s_z & t\tau_z s_0 & 0 & 0 & \cdots \\ 0 & 0 & 0 & -2\lambda_{so}\tau_0 s_z & 0 & 0 & \cdots \\ \vdots & \vdots & \vdots & \vdots & \vdots & \vdots & \ddots \end{pmatrix}, \quad (\text{S22})$$

As τ_z and s_z also commute with \mathcal{H}_1 , the zero-energy eigenvectors of \mathcal{H}_1 can also be assigned the form

$$|\Psi_{\tau s}\rangle = |\tau_z = \tau\rangle \otimes |s_z = s\rangle \otimes (\psi_{1B}, \psi_{2A}, \psi_{2B}, \psi_{3A}, \psi_{3B}, \dots, \psi_{nA}, \psi_{nB}, \dots)^T. \quad (\text{S23})$$

Accordingly, the eigenvalue equation $\mathcal{H}_1|\Psi_{\tau s}\rangle = 0$ leads to the following equations with periodic structures,

$$\begin{aligned} 2\lambda_{so,s}\psi_{2B} &= 0, \\ t_\tau\psi_{2B} - 2\lambda_{so,s}\psi_{3A} &= 0, \\ 2\lambda_{so,s}\psi_{1B} + t_\tau\psi_{2A} + 2\lambda_{so,s}\psi_{3B} &= 0, \\ -2\lambda_{so,s}\psi_{2A} + t_\tau\psi_{3B} - 2\lambda_{so,s}\psi_{4A} &= 0, \\ \dots \\ 2\lambda_{so,s}\psi_{(n-1)B} + t_\tau\psi_{nA} + 2\lambda_{so,s}\psi_{(n+1)B} &= 0, \\ -2\lambda_{so,s}\psi_{nA} + t_\tau\psi_{(n+1)B} - 2\lambda_{so,s}\psi_{(n+2)A} &= 0, \\ \dots \end{aligned} \quad (\text{S24})$$

It is readily found that the components of eigenvectors have $\psi_{(2n)B} = \psi_{(2n+1)A} = 0$. Therefore, we only need to focus on the following equations,

$$\begin{aligned} 2\lambda_{so,s}\psi_{(2n-1)B} + t_\tau\psi_{(2n)A} + 2\lambda_{so,s}\psi_{(2n+1)B} &= 0, \\ -2\lambda_{so,s}\psi_{(2n)A} + t_\tau\psi_{(2n+1)B} - 2\lambda_{so,s}\psi_{(2n+2)A} &= 0. \end{aligned} \quad (\text{S25})$$

Consider the trial function

$$\begin{pmatrix} \psi_{(2n+1)B} \\ \psi_{(2n+2)A} \end{pmatrix} = \xi^n \begin{pmatrix} \psi_{1B} \\ \psi_{2A} \end{pmatrix}, \quad (\text{S26})$$

where $|\xi| < 1$ is required so that the wave function decays in space and corresponds to a bound state. Accordingly, one finds that the series of equations reduce to two algebra equations, which read

$$\begin{aligned} 2\lambda_{so,s}\psi_{1B} + t_\tau\psi_{2A} + 2\lambda_{so,s}\xi\psi_{1B} &= 0, \\ -2\lambda_{so,s}\psi_{2A} + t_\tau\xi\psi_{1B} - 2\lambda_{so,s}\xi\psi_{2A} &= 0. \end{aligned} \quad (\text{S27})$$

By simple algebra, one finds

$$\begin{aligned} \psi_{1B} &= -\frac{t_\tau}{2\lambda_{so,s}(1+\xi)}\psi_{2A}, \\ \frac{2\lambda_{so,s}(1+\xi)}{t_\tau\xi} &= -\frac{t_\tau}{2\lambda_{so,s}(1+\xi)}. \end{aligned} \quad (\text{S28})$$

There are two solutions for ξ ,

$$\xi_{\pm} = \frac{-(t_\tau^2 + 8\lambda_{so,s}^2) \pm \sqrt{t_\tau^2(t_\tau^2 + 16\lambda_{so,s}^2)}}{8\lambda_{so,s}^2}, \quad (\text{S29})$$

however, only ξ_+ leads to decaying wave functions, so bound states. Taking ξ_+ back into Eq.(S28), one finds

$$\psi_{1B} = \frac{4t_\tau\lambda_{so,s}^2}{\lambda_{so,s}(t_\tau^2 - \sqrt{t_\tau^2(t_\tau^2 + 16\lambda_{so,s}^2)})}\psi_{2A} \equiv \eta_{\tau s}\psi_{2A} = -\tau s|\eta_{\tau s}|\psi_{2A}. \quad (\text{S30})$$

As τ and s have four possible combinations, there are also four eigenvectors corresponding to four zero-energy bound states. The eigenvectors can also be expressed as

$$|\Psi_{\tau s}\rangle = |\tau_z = \tau\rangle \otimes |s_z = s\rangle \otimes \mathcal{N}(\eta_{\tau s}, 1, 0, 0, \xi_+ \eta_{\tau s}, \xi_+, 0, 0, \xi_+^2 \eta_{\tau s}, \xi_+^2, \dots)^T. \quad (\text{S31})$$

The normalization condition $\langle \Psi_{\tau s} | \Psi_{\tau s} \rangle = 1$ gives

$$\mathcal{N}^2 (1 + \eta_{\tau s}^2) \sum_{n=0}^{\infty} \xi_+^{2n} = \mathcal{N}^2 \frac{(1 + \eta_{\tau s}^2)}{1 - \xi_+^2} = 1, \quad (\text{S32})$$

which indicates

$$\mathcal{N} = \sqrt{\frac{1 - \xi_+^2}{1 + \eta_{\tau s}^2}}. \quad (\text{S33})$$

Let us now analyze the effect of \mathcal{H}_2 . For the first two terms in \mathcal{H}_2 , $\mathcal{H}_{2,12} = -\sqrt{3}tq'_x \cos \frac{k_y}{2} \tau_z s_0 \sigma_x + \sqrt{3}tq'_x \sin \frac{k_y}{2} \tau_z s_0 \sigma_y$, the corresponding matrix form reads

$$\mathcal{H}_{2,12} = \begin{pmatrix} 0 & -\sqrt{3}tq'_x \tau_z s_0 & 0 & 0 & 0 & 0 & \cdots \\ -\sqrt{3}tq'_x \tau_z s_0 & 0 & 0 & 0 & 0 & 0 & \cdots \\ 0 & 0 & 0 & -\sqrt{3}tq'_x \tau_z s_0 & 0 & 0 & \cdots \\ 0 & 0 & -\sqrt{3}tq'_x \tau_z s_0 & 0 & 0 & 0 & \cdots \\ 0 & 0 & 0 & 0 & 0 & -\sqrt{3}tq'_x \tau_z s_0 & \cdots \\ 0 & 0 & 0 & 0 & -\sqrt{3}tq'_x \tau_z s_0 & 0 & \cdots \\ \vdots & \vdots & \vdots & \vdots & \vdots & \vdots & \ddots \end{pmatrix}. \quad (\text{S34})$$

By projecting $\mathcal{H}_{2,12}$ onto $\{|\Psi_{\tau s}\rangle\}$, one finds its contribution to the boundary Hamiltonian, which reads

$$\begin{aligned} (\mathcal{H}_{zigzag,1})_{\tau s, \tau' s'} &= \langle \Psi_{\tau s}^\dagger | \mathcal{H}_{2,12} | \Psi_{\tau' s'} \rangle \\ &= -2\sqrt{3}tq'_x \tau \eta_{\tau s} \delta_{\tau \tau'} \delta_{ss'} \mathcal{N}^2 \sum_{n=0}^{\infty} \xi_+^{2n} \\ &= -\frac{2\sqrt{3}t\tau \eta_{\tau s}}{1 + \eta_{\tau s}^2} q'_x \delta_{\tau \tau'} \delta_{ss'} \\ &= \frac{2\sqrt{3}t|\eta_{\tau s}|}{1 + \eta_{\tau s}^2} s q'_x \delta_{\tau \tau'} \delta_{ss'}. \end{aligned} \quad (\text{S35})$$

Above in the last step, we have used the facts $\eta_{\tau s} = -\tau s |\eta_{\tau s}|$ and $\tau^2 = 1$. Also choosing the basis to be $(|\Psi_{11}\rangle, |\Psi_{1-1}\rangle, |\Psi_{-11}\rangle, |\Psi_{-1-1}\rangle)^T$, then $\mathcal{H}_{zigzag,1}$ can be expressed in terms of the Pauli matrices as

$$\mathcal{H}_{zigzag,1} = \frac{2\sqrt{3}t|\eta_{\tau s}|}{1 + \eta_{\tau s}^2} q'_x \tau_0 s_z. \quad (\text{S36})$$

For the third term, $\mathcal{H}_{2,3} = -2\sqrt{3}\lambda_{so}q'_x \tau_0 s_z \sigma_z$, its matrix form reads

$$\mathcal{H}_{2,3} = \tau_0 \otimes s_z \otimes \begin{pmatrix} 2\sqrt{3}\lambda_{so}q'_x & 0 & 0 & 0 & 0 & 0 & \cdots \\ 0 & -2\sqrt{3}\lambda_{so}q'_x & 0 & 0 & 0 & 0 & \cdots \\ 0 & 0 & 2\sqrt{3}\lambda_{so}q'_x & 0 & 0 & 0 & \cdots \\ 0 & 0 & 0 & -2\sqrt{3}\lambda_{so}q'_x & 0 & 0 & \cdots \\ 0 & 0 & 0 & 0 & 2\sqrt{3}\lambda_{so}q'_x & 0 & \cdots \\ 0 & 0 & 0 & 0 & 0 & -2\sqrt{3}\lambda_{so}q'_x & \cdots \\ \vdots & \vdots & \vdots & \vdots & \vdots & \vdots & \ddots \end{pmatrix}. \quad (\text{S37})$$

Its contribution to the boundary Hamiltonian can be similarly determined, which takes the form

$$\begin{aligned} (\mathcal{H}_{zigzag,2})_{\tau s, \tau' s'} &= \langle \Psi_{\tau s}^\dagger | \mathcal{H}_{2,3} | \Psi_{\tau' s'} \rangle \\ &= 2\sqrt{3}\lambda_{so} s q'_x (\eta_{\tau s}^2 - 1) \mathcal{N}^2 \sum_{n=0}^{\infty} \xi_+^{2n} \delta_{\tau \tau'} \delta_{ss'} \\ &= \frac{2\sqrt{3}\lambda_{so}(\eta_{\tau s}^2 - 1)s}{1 + \eta_{\tau s}^2} q'_x \delta_{\tau \tau'} \delta_{ss'}. \end{aligned} \quad (\text{S38})$$

Also in terms of the Pauli matrices, its form can be expressed as

$$\mathcal{H}_{zigzag,2} = \frac{2\sqrt{3}\lambda_{so}(\eta_{\tau s}^2 - 1)}{1 + \eta_{\tau s}^2} q'_x \tau_0 s_z. \quad (\text{S39})$$

A combination of the two contributions gives the full expression for the linear momentum term in the boundary Dirac Hamiltonian. For the chemical potential term, its contribution is also simply

$$\mathcal{H}_{zigzag,3} = -\mu \tau_z s_0. \quad (\text{S40})$$

Let us now analyze the contribution from the last piece, the pairing term $\mathcal{H}_{2,5} = -[\Delta_0 + 2\Delta_2(-1 - \sqrt{3}q'_x \cos \frac{3k_y}{2})]\tau_y s_y \sigma_0$. Its explicit matrix form is

$$\mathcal{H}_{2,5} = \begin{pmatrix} -(\Delta_0 - 2\Delta_2)\tau_y s_y & 0 & \sqrt{3}\Delta_2 q'_x \tau_y s_y & 0 & \cdots \\ 0 & -(\Delta_0 - 2\Delta_2)\tau_y s_y & 0 & \sqrt{3}\Delta_2 q'_x \tau_y s_y & \cdots \\ \sqrt{3}\Delta_2 q'_x \tau_y s_y & 0 & -(\Delta_0 - 2\Delta_2)\tau_y s_y & 0 & \cdots \\ 0 & \sqrt{3}\Delta_2 q'_x \tau_y s_y & 0 & -(\Delta_0 - 2\Delta_2)\tau_y s_y & \cdots \\ \vdots & \vdots & \vdots & \vdots & \ddots \end{pmatrix}. \quad (\text{S41})$$

Its contribution to the boundary Hamiltonian is

$$\begin{aligned} (\mathcal{H}_{zigzag,4})_{\tau s, \tau' s'} &= \langle \Psi_{\tau s} | \mathcal{H}_{2,5} | \Psi_{\tau' s'} \rangle \\ &= -(\Delta_0 - 2\Delta_2)(\tau_y)_{\tau \tau'} (s_y)_{ss'} + \sqrt{3}\Delta_2 q'_x (\tau_y)_{\tau \tau'} (s_y)_{ss'} \mathcal{N}^2 \sum_{n=1}^{+\infty} 2[\psi_{nB} \psi_{(n+1)B} + \psi_{(n+1)A} \psi_{(n+2)A}] \\ &= -(\Delta_0 - 2\Delta_2)(\tau_y)_{\tau \tau'} (s_y)_{ss'}. \end{aligned} \quad (\text{S42})$$

In the last step, we have used the fact that the products $\psi_{nB} \psi_{(n+1)B}$ and $\psi_{nA} \psi_{(n+1)A}$ are always zero as $\psi_{(2n+1)A} = \psi_{2nB} = 0$. In terms of the Pauli matrices,

$$\mathcal{H}_{zigzag,4} = -(\Delta_0 - 2\Delta_2)\tau_y s_y. \quad (\text{S43})$$

Taking all contribution together, we reach the final expression for the boundary Hamiltonian for the upper zigzag edge, which reads

$$\mathcal{H}_{zigzag} = \sum_{i=1}^4 \mathcal{H}_{zigzag,i} = v' q'_x \tau_0 s_z - \mu \tau_z s_0 - (\Delta_0 - 2\Delta_2)\tau_y s_y, \quad (\text{S44})$$

where

$$v' = \left[\frac{2\sqrt{3}t|\eta_{\tau s}| + 2\sqrt{3}\lambda_{so}(\eta_{\tau s}^2 - 1)}{1 + \eta_{\tau s}^2} \right]. \quad (\text{S45})$$

When $\lambda_{so} \ll t$, one can do an expansion of $\eta_{\tau s}$ about λ_{so}/t . Only keeping the leading-order term, the result is

$$\begin{aligned} |\eta_{\tau,s}| &= \frac{4t\lambda_{so}^2}{\lambda_{so}(\sqrt{t^2(t^2 + 16\lambda_{so}^2)} - t^2)} \\ &\approx \frac{4t\lambda_{so}^2}{\lambda_{so}(t^2 + 8\lambda_{so}^2 - t^2)} \\ &= \frac{t}{2\lambda_{so}}. \end{aligned} \quad (\text{S46})$$

When $\lambda_{so} \ll t$, $|\eta_{\tau,s}| \gg 1$, so $\eta_{\tau s}^2 \pm 1 \approx \eta_{\tau s}^2$, one finds

$$\begin{aligned} v' &= \frac{2\sqrt{3}t|\eta_{\tau s}| + 2\sqrt{3}\lambda_{so}(\eta_{\tau s}^2 - 1)}{1 + \eta_{\tau s}^2} \\ &\approx \frac{2\sqrt{3}t|\eta_{\tau s}| + 2\sqrt{3}\lambda_{so}\eta_{\tau s}^2}{\eta_{\tau s}^2} \\ &\approx 6\sqrt{3}\lambda_{so}. \end{aligned} \quad (\text{S47})$$

In the limit $\mu = 0$, the boundary Hamiltonian reduces to the form of Eq.(9) in the main text. By comparing the analytical results with the numerical results, we find that the above low-energy boundary Hamiltonian gives a very accurate description of the physics on the zigzag edge.

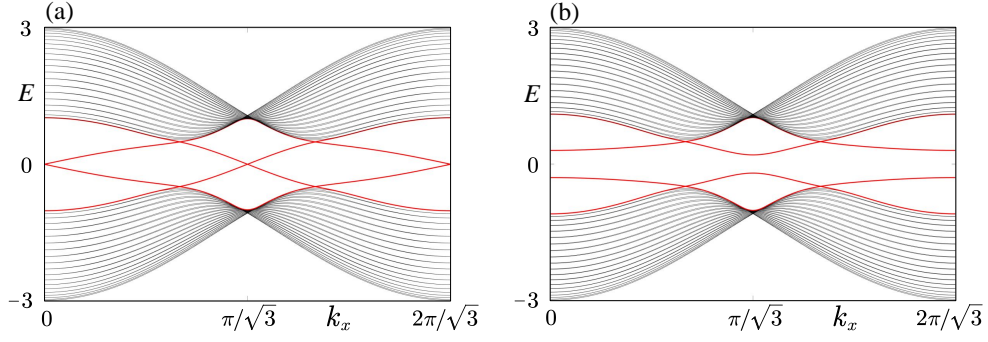


FIG. S1: (Color online) Energy spectrum for the Kane-Mele model with d-wave pairing. A cylindrical geometry is considered, with periodic boundary condition in the x direction and open boundary condition in the y direction. The upper y -normal boundary is a beard edge, and the lower y -normal boundary is a zigzag edge. Chosen parameters are $t = 1$, $\lambda_{so} = 0.1$, $\mu = 0$. In (a), $\Delta_1 = 0.1$ and $\Delta_2 = 0$, the boundary Dirac points at time-reversal invariant momenta turn out to be robust against the nearest-neighbor pairing. In (b), $\Delta_1 = 0$ and $\Delta_2 = 0.1$, the boundary Dirac points are gapped by the next-nearest-neighbor pairing.

II. TWO-DIMENSIONAL HONEYCOMB-LATTICE TOPOLOGICAL INSULATORS IN PROXIMITY TO D-WAVE SUPERCONDUCTORS

In the main text, we have used the isotropic extended s-wave pairing to illustrate the physics. To show explicitly that the physics does not rely on a specific pairing type, in this section we consider the d-wave pairing, a pairing type widely believed to be relevant to high- T_c cuprate-based superconductors. On a honeycomb lattice, the pairing amplitude of the d-wave pairing follows the pattern $\Delta_{\alpha,ij} = \Delta_\alpha \cos 2\theta_{ij}$, with θ_{ij} denoting the angle that the bond vector \mathbf{d}_{ij} is in regard to the x direction. Accordingly, the Kane-Mele model with d-wave pairing up to the next-nearest neighbors reads

$$\begin{aligned} \mathcal{H}_{\text{BdG}}(\mathbf{k}) = & t(2 \cos \frac{\sqrt{3}k_x}{2} \cos \frac{k_y}{2} + \cos k_y) \tau_z s_0 \sigma_x - t(2 \cos \frac{\sqrt{3}k_x}{2} \sin \frac{k_y}{2} - \sin k_y) \tau_z s_0 \sigma_y \\ & + 2\lambda_{so}(\sin \sqrt{3}k_x - 2 \sin \frac{\sqrt{3}k_x}{2} \cos \frac{3k_y}{2}) \tau_0 s_z \sigma_z - \mu \tau_z s_0 \sigma_0 \\ & - \Delta_1(\cos \frac{\sqrt{3}k_x}{2} \cos \frac{k_y}{2} - \cos k_y) \tau_y s_y \sigma_x + \Delta_1(\cos \frac{\sqrt{3}k_x}{2} \sin \frac{k_y}{2} + \sin k_y) \tau_y s_y \sigma_y \\ & - 2\Delta_2(\cos \sqrt{3}k_x - \cos \frac{\sqrt{3}k_x}{2} \cos \frac{3k_y}{2}) \tau_y s_y \sigma_0. \end{aligned} \quad (\text{S48})$$

Similar to the extended s-wave pairing, we find that the nearest-neighbor pairing also has a negligible effect to the helical edge states, and only the next-nearest-neighbor pairing can open a gap to the boundary Dirac points, as shown in Fig.S1. Therefore, below we also set $\Delta_1 = 0$ for simplicity. In parallel to the extended s-wave pairing case, we first derive the corresponding low-energy boundary Hamiltonian for both beard and zigzag edges, and then numerically show the realization of Majorana Kramers pairs at the sublattice domain walls once the topological criterion is fulfilled.

II. A. Low-energy boundary Hamiltonian for the beard edge

Compared to the extended s-wave pairing case, since only the pairing term has been changed, what we need to concern is just the change of Dirac mass. For the beard edge, as aforementioned the expansion of the Hamiltonian is around $k_x = 0$. Also only remaining terms up to the linear order in momentum, the Hamiltonian reads

$$\begin{aligned} \mathcal{H}_{\text{BdG}}(q_x, k_y) = & t(2 \cos \frac{k_y}{2} + \cos k_y) \tau_z s_0 \sigma_x - t(2 \sin \frac{k_y}{2} - \sin k_y) \tau_z s_0 \sigma_y \\ & + 2\sqrt{3}\lambda_{so}q_x(1 - \cos \frac{3k_y}{2}) \tau_0 s_z \sigma_z - \mu \tau_z s_0 \sigma_0 \\ & - 2\Delta_2(1 - \cos \frac{3k_y}{2}) \tau_y s_y \sigma_0, \end{aligned} \quad (\text{S49})$$

where the last line corresponds to the pairing term at the neighborhood of $k_x = 0$. Focusing on the last line, its matrix form in the underlying basis $\Psi_{q_x} = (c_{1,A,q_x}, c_{1,B,q_x}, c_{2,A,q_x}, c_{2,B,q_x}, \dots, c_{n,A,q_x}, c_{n,B,q_x}, \dots)^T$ is

$$\mathcal{H}_{dSC} = \begin{pmatrix} -2\Delta_2\tau_y s_y & 0 & \Delta_2\tau_y s_y & 0 & \cdots \\ 0 & -2\Delta_2\tau_y s_y & 0 & \Delta_2\tau_y s_y & \cdots \\ \Delta_2\tau_y s_y & 0 & -2\Delta_2\tau_y s_y & 0 & \cdots \\ 0 & \Delta_2\tau_y s_y & 0 & -2\Delta_2\tau_y s_y & \cdots \\ \vdots & \vdots & \vdots & \vdots & \ddots \end{pmatrix}. \quad (\text{S50})$$

Also taking this term as a perturbation and projecting it onto the subspace spanned by the four eigenvectors $|\Psi_{\tau s}\rangle$, where

$$|\Psi_{\tau s}\rangle = |\tau_z = \tau\rangle \otimes |s_z = s\rangle \otimes \frac{\sqrt{3}}{2}(1, 0, -\frac{1}{2}, 0, \dots, (-\frac{1}{2})^{(n-1)}, 0, \dots)^T, \quad (\text{S51})$$

one finds that its contribution is

$$\begin{aligned} (\mathcal{H}_{beard,3})_{\tau s, \tau' s'} &= \langle \Psi_{\tau s} | \mathcal{H}_{dSC} | \Psi_{\tau' s'} \rangle \\ &= -2\Delta_2(\tau_y)_{\tau\tau'}(s_y)_{ss'} - \Delta_2(\tau_y)_{\tau\tau'}(s_y)_{ss'} \\ &= -3\Delta_2(\tau_y)_{\tau\tau'}(s_y)_{ss'}. \end{aligned} \quad (\text{S52})$$

In terms of the Pauli matrices, its form is

$$\mathcal{H}_{beard,3} = -3\Delta_2\tau_y s_y. \quad (\text{S53})$$

Replacing the Dirac mass term in Eq.(S19) by the above Dirac mass term, one gets

$$\mathcal{H}_{beard} = vq_x\tau_0 s_z - \mu\tau_z s_0 - 3\Delta_2\tau_y s_y. \quad (\text{S54})$$

This is the low-energy boundary Hamiltonian for the beard edge when the pairing is d-wave type.

II. B. Low-energy boundary Hamiltonian for the zigzag edge

For zigzag edge and d-wave pairing, an expansion of the Hamiltonian around $k_x = \pi/\sqrt{3}$ up to the linear order in momentum gives

$$\begin{aligned} \mathcal{H}_{BdG}(q'_x, k_y) &= t(-\sqrt{3}q'_x \cos \frac{k_y}{2} + \cos k_y)\tau_z s_0 \sigma_x + t(\sqrt{3}q'_x \sin \frac{k_y}{2} + \sin k_y)\tau_z s_0 \sigma_y \\ &\quad + 2\lambda_{so}(-\sqrt{3}q'_x - 2 \cos \frac{3k_y}{2})\tau_0 s_z \sigma_z - \mu\tau_z s_0 \sigma_0 \\ &\quad - 2\Delta_2(-1 + \frac{\sqrt{3}}{2}q'_x \cos \frac{3k_y}{2})\tau_y s_y \sigma_0. \end{aligned} \quad (\text{S55})$$

where the last line corresponds to the pairing term at the neighborhood of $k_x = \pi/\sqrt{3}$.

In the basis $\Psi_{q'_x} = (c_{1,B,q'_x}, c_{2,A,q'_x}, c_{2,B,q'_x}, c_{3,A,q'_x}, c_{3,B,q'_x}, \dots, c_{n,A,q'_x}, c_{n,B,q'_x}, \dots)^T$, the matrix form of the pairing term reads

$$\mathcal{H}_{dSC} = \begin{pmatrix} 2\Delta_2\tau_y s_y & 0 & -\frac{\sqrt{3}}{2}\Delta_2q'_x\tau_y s_y & 0 & \cdots \\ 0 & 2\Delta_2\tau_y s_y & 0 & -\frac{\sqrt{3}}{2}\Delta_2q'_x\tau_y s_y & \cdots \\ -\frac{\sqrt{3}}{2}\Delta_2q'_x\tau_y s_y & 0 & 2\Delta_2\tau_y s_y & 0 & \cdots \\ 0 & -\frac{\sqrt{3}}{2}\Delta_2q'_x\tau_y s_y & 0 & 2\Delta_2\tau_y s_y & \cdots \\ \vdots & \vdots & \vdots & \vdots & \ddots \end{pmatrix}. \quad (\text{S56})$$

Also taking this term as a perturbation and projecting it onto the subspace spanned by the four eigenvectors $|\Psi_{\tau s}\rangle$, where

$$|\Psi_{\tau s}\rangle = |\tau_z = \tau\rangle \otimes |s_z = s\rangle \otimes \mathcal{N}(\eta_{\tau s}, 1, 0, 0, \xi_+ \eta_{\tau s}, \xi_+, 0, 0, \xi_+^2 \eta_{\tau s}, \xi_+^2, \dots)^T \quad (\text{S57})$$

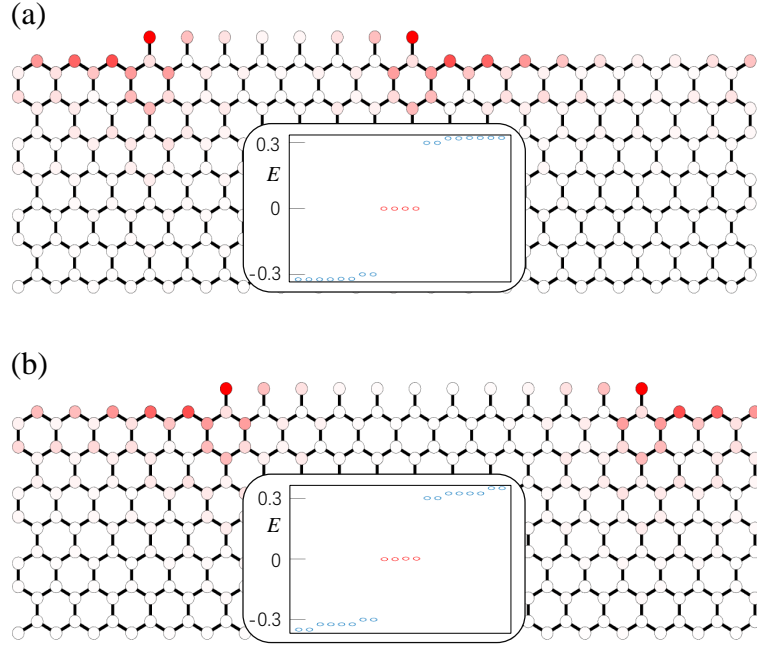


FIG. S2: (Color online) Majorana Kramers pairs at sublattice domain walls on the upper boundary. The lattice geometry is cylindrical with periodic boundary condition in the x direction except for the upper most beard-edge part (left and right edges are considered to be connected in our numerical calculations). Throughout this work, the same boundary conditions are applied to all similar lattice geometries, below the boundary conditions will no longer be emphasized when similar lattice geometries are present. Chosen parameters in (a) and (b) are $t = 1$, $\lambda_{so} = 0.1$, $\mu = 0$, $\Delta_1 = 0$, $\Delta_2 = 0.15$, and the considered lattice geometry and size are shown explicitly. The insets on top of the underlying lattices correspond to the energy spectrum. Here we have only shown the part of eigenvalues closest to zero energy. The middle four dots in red indicate the existence of two Majorana Kramers pairs. The shade of red color on the lattice sites reflect the weight of the probability density ($|\psi(x, y)|^2$) of Majorana Kramers pairs.

with ξ , $\eta_{\tau s}$ and \mathcal{N} given by Eqs.(S29), (S30) and (S33), respectively, one finds that its contribution is

$$\begin{aligned} (\mathcal{H}_{zigzag,5})_{\tau s, \tau' s'} &= \langle \Psi_{\tau s} | \mathcal{H}_{dSC} | \Psi_{\tau' s'} \rangle \\ &= 2\Delta_2 (\tau_y)_{\tau \tau'} (s_y)_{ss'}. \end{aligned} \quad (\text{S58})$$

In terms of the Pauli matrices, its form can be expressed as

$$\mathcal{H}_{zigzag,5} = 2\Delta_2 \tau_y s_y. \quad (\text{S59})$$

Replacing the Dirac mass term in Eq.(S19) by the above Dirac mass term, one gets

$$\mathcal{H}_{zigzag} = v' q'_x \tau_0 s_z - \mu \tau_z s_0 + 2\Delta_2 \tau_y s_y. \quad (\text{S60})$$

This is the low-energy boundary Hamiltonian for the zigzag edge when the pairing is d-wave type.

II. C. Majorana Kramers pairs at sublattice domain walls on the upper boundary

Let us focus on the special case with $\mu = 0$. According to the low-energy boundary Hamiltonian for both beard and zigzag edges, one knows that if the upper boundary becomes nonuniform and consists of two parts which respectively terminate at A and B sublattices, the corresponding low-energy boundary Hamiltonian, due to the further breaking of translation symmetry in the x direction, will become

$$\mathcal{H} = -iv(x)\partial_x \tau_0 s_z + m(x)\tau_y s_y, \quad (\text{S61})$$

where $v(x) = v$, $m(x) = -3\Delta_2$ if the part corresponds to a beard edge, and $v(x) = v'$, $m(x) = 2\Delta_2$ if the part corresponds to a zigzag edge. The velocities in both parts have the same sign, but the Dirac masses have opposite signs, as a result, the sublattice

domain walls correspond to domain walls of Dirac mass as long as $\Delta_2 \neq 0$. This conclusion suggests that the sublattice domain walls will bind Majorana Kramers pairs if the next-nearest-neighboring pairing is finite. Through numerical calculations, we confirm the appearance of Majorana Kramers pairs at the sublattice domain walls, as shown in Fig.S2. The results in this section demonstrate that the emergence of Majorana zero modes at sublattice domain walls is not restricted to certain specific pairing type.

Before ending this section, we say some more words on the pairing for the realization of sublattice-sensitive Majorana Kramers pairs (time-reversal invariant case) or Majorana zero modes (time-reversal symmetry breaking case). When time-reversal symmetry is preserved, it is known that a uniform on-site s-wave pairing cannot realize any topological superconducting phase [1]. Accordingly, as long as the time-reversal symmetry is preserved, to realize Majorana Kramers pairs the superconductivity must be somewhat unconventional in some sense, like being momentum dependent, odd-parity or space dependent. The extended s-wave pairing discussed in the main text and the d-wave pairing discussed above belong to the momentum-dependent case. If the pairing is space-dependent, Majorana Kramers pairs can be achieved even though the pairing is purely on-site. To see this, let us take the simplest case for illustration. The simplest space-dependent pairing is a staggered s-wave pairing (appearing as a term of the form $-\Delta_0 \tau_y s_y \sigma_z$ in the BdG Hamiltonian), that is, the s-wave pairing is purely on-site but takes opposite signs on the sublattice A and sublattice B. By applying the low-energy boundary theory, one easily finds that the low-energy Hamiltonians for the beard and zigzag edges are respectively given by

$$\begin{aligned}\mathcal{H}_{beard} &= vq_x \tau_0 s_z - \mu \tau_z s_0 - \Delta_0 \tau_y s_y, \\ \mathcal{H}_{zigzag} &= v'q'_x \tau_0 s_z - \mu \tau_z s_0 + \Delta_0 \frac{\eta_{\tau s}^2 - 1}{\eta_{\tau s}^2 + 1} \tau_y s_y.\end{aligned}\quad (\text{S62})$$

As $\eta_{\tau s}^2 > 1$, it is readily seen that Dirac masses induced by the pairing on the two kinds of edges have opposite signs, accordingly Majorana Kramers pairs will emerge at the sublattice domain walls on the edge. When introducing a Zeeman field (which can be induced by an external magnetic field or a ferromagnet insulator in contact) to break the time-reversal symmetry, the requirement on unconventional superconductivity can accordingly be released, and the on-site s-wave pairing is sufficient for the realization of sublattice-sensitive Majorana zero modes. The underlying reason is that the Zeeman field will induce a Dirac mass competing with the Dirac mass induced by superconductivity. Interestingly, one can find via the low-energy boundary theory that the sublattice terminations also affect the Dirac mass induced by Zeeman field. When the beard and zigzag are dominated by different Dirac masses, Majorana zero modes will emerge at the sublattice domain walls. In short, the realization of Majorana zero modes at sublattice domain walls does not rely on certain specific pairing type.

III. THE IMPACT OF FINITE CHEMICAL POTENTIAL ON THE TOPOLOGICAL CRITERION

Above we have restricted to the $\mu = 0$ case for illustration. As the robustness of Majorana Kramers pairs is protected by non-spatial particle-hole symmetry and the chemical potential term does not break this symmetry, the Majorana Kramers pairs will remain robust as long as the chemical potential is lower than a critical value. Before proceeding, it is worth noting that in this work we consider that the superconductivity in the two-dimensional topological insulator is induced by proximity effect. Accordingly, the chemical potential is not required to cross the bulk conduction or valence band to guarantee a metallic normal state to achieve superconductivity.

Since the Majorana Kramers pairs have codimension $d_c = 2$, the critical chemical potential corresponds to the value at which a boundary topological phase transition occurs. At the critical point of a boundary topological phase transition, the boundary energy gap vanishes, while the bulk energy gap can remain open. We can first give an estimate of the critical value through the low-energy boundary Hamiltonian. According to Eqs.(S19) and (S44), the Dirac mass changes sign from $k_x = 0$ to $k_x = \pi/\sqrt{3}$ when $|\Delta_2| > |\Delta_0|/2 > 0$. It indicates that there exists a node between 0 and $\pi/\sqrt{3}$. Furthermore, as the Δ_2 -term cannot open a gap at $k_x = 0$ and the Δ_0 -term opens an equal gap at $k_x = 0$ and $k_x = \pi/\sqrt{3}$, according to the tight-binding form of the pairing term in Eq.(S3), the Dirac mass induced by the on-site and next-nearest-neighbor pairings on the boundary can be approximated as

$$m(k_x) \approx -\Delta_0 + 2\Delta_2(\cos \sqrt{3}k_x - \cos \frac{\sqrt{3}}{2}k_x). \quad (\text{S63})$$

For the parameters considered in the main text, $\Delta_0 = \Delta_2 = 0.3$, the node determined by the above formula is located at $k_{x,n} \simeq 0.73$. Since this momentum is closer to $k_x = 0$ than to $k_x = \pi/\sqrt{3}$, we can focus on the low-energy boundary Hamiltonian for the beard edge shown in Eq.(S19), whose energy spectrum is

$$E = \pm \sqrt{(3\sqrt{3}\lambda_{so}q_x \pm \mu)^2 + m^2(q_x)}. \quad (\text{S64})$$

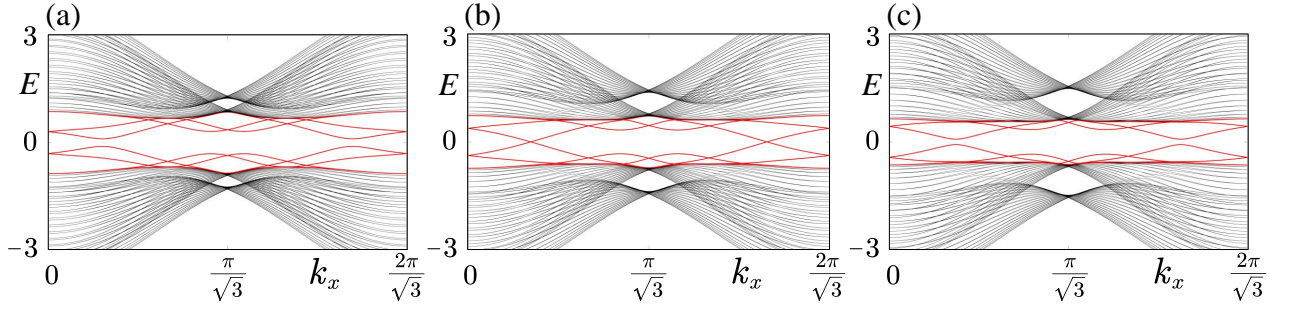


FIG. S3: (Color online) The evolution of boundary energy gap with respect to μ . A cylindrical geometry is considered, with periodic boundary condition in the x direction and open boundary condition in the y direction. The upper y -normal boundary is a beard edge, and the lower y -normal boundary is a zigzag edge. Here the extended s-wave pairing is considered. Chosen parameters are $t = 1$, $\lambda_{so} = 0.1$, $\Delta_0 = \Delta_2 = 0.3$, $\Delta_1 = 0$. (a) $\mu = 0.2$, the mid-gap red lines show the existence of a finite gap in the boundary energy spectrum. (b) $\mu = 0.345$, the boundary energy gap vanishes, corresponding to the critical point of a boundary topological phase transition. (c) $\mu = 0.45$, a gap is reopened in the boundary energy spectrum.

Accordingly, the critical chemical potential is approximately given by

$$\mu_c \approx 3\sqrt{3}\lambda_{so}k_{x,n} \simeq 3.8\lambda_{so}. \quad (\text{S65})$$

For $\lambda_{so} = 0.1$, $\mu_c \approx 0.38$. In Fig.S3, the evolution of boundary energy gap with respect to μ is shown. Fig.S3(b) shows that the precise value of μ_c for the given set of parameters is 0.345, quite close to the estimated value. The formula in Eq.(S65) indicates that a stronger spin-orbit coupling admits a larger range of chemical potential within which the sublattice domain walls can host Majorana Kramers pairs.

In Fig.S4, the numerical results confirm that the Majorana Kramers pairs are robust against the increase of chemical potential as long as its value remains lower than the critical value.

IV. SUBLATTICE-SENSITIVE MAJORANA MODES IN TIME-REVERSAL SYMMETRY BROKEN SYSTEMS

So far, we have restricted to time-reversal invariant cases. In this section, we consider the introduction of an in-plane magnetic field to break the time-reversal symmetry. To be specific, we consider that the magnetic field is applied in the x direction, in parallel to the domain walls on the upper boundary. The magnetic field will contribute a Zeeman splitting term of the form $B_x\tau_zs_x\sigma_0$ (g -factor and Bohr magneton are absorbed in B_x for notational simplicity) to the Hamiltonian. Also treating this term as a perturbation, since this term contains σ_0 in the sublattice subspace, one can easily find that it will contribute a Dirac mass term of the form $B_x\tau_zs_x$ for both beard and zigzag edges. For generality, let us assume that the Dirac mass induced by superconductivity on the beard edge is of the form $m_b\tau_ys_y$ and that on the zigzag edge is of the form $m_z\tau_ys_y$. Taking into account the contribution from the Zeeman field, the corresponding low-energy boundary Hamiltonians are

$$\begin{aligned} H_{beard} &= vq_x\tau_0s_z - \mu\tau_zs_0 + m_b\tau_ys_y + B_x\tau_zs_x, \\ H_{zigzag} &= v'q'_x\tau_0s_z - \mu\tau_zs_0 + m_z\tau_ys_y + B_x\tau_zs_x. \end{aligned} \quad (\text{S66})$$

Similar to the chemical potential, the Zeeman field will induce a boundary topological phase transition when it induces a gap closure in the boundary energy spectrum. According to the boundary energy spectrum,

$$\begin{aligned} E_{beard}(q_x) &= \pm\sqrt{v^2q_x^2 + \mu^2 + m_b^2 + B_x^2 \pm 2\sqrt{\mu^2v^2q_x^2 + B_x^2(\mu^2 + m_b^2)}}, \\ E_{zigzag}(q'_x) &= \pm\sqrt{v'^2q_x'^2 + \mu^2 + m_z^2 + B_x^2 \pm 2\sqrt{\mu^2v'^2q_x'^2 + B_x^2(\mu^2 + m_z^2)}}. \end{aligned} \quad (\text{S67})$$

For both beard and zigzag edges, the boundary energy gaps will get closed at the time-reversal invariant momentum, i.e., $q_x = 0$, $q'_x = 0$. For the beard edge, the closure of boundary energy gap occurs when $|B_x| = B_{b,c} \equiv \sqrt{\mu^2 + m_b^2}$. For the zigzag edge, the condition is similar, that is, $|B_x| = B_{z,c} \equiv \sqrt{\mu^2 + m_z^2}$. The critical conditions for the two types of edges indicate that if the Zeeman field is chosen to satisfy $\min\{B_{b,c}, B_{z,c}\} < B_x < \max\{B_{b,c}, B_{z,c}\}$, the system will enter a new topological phase on

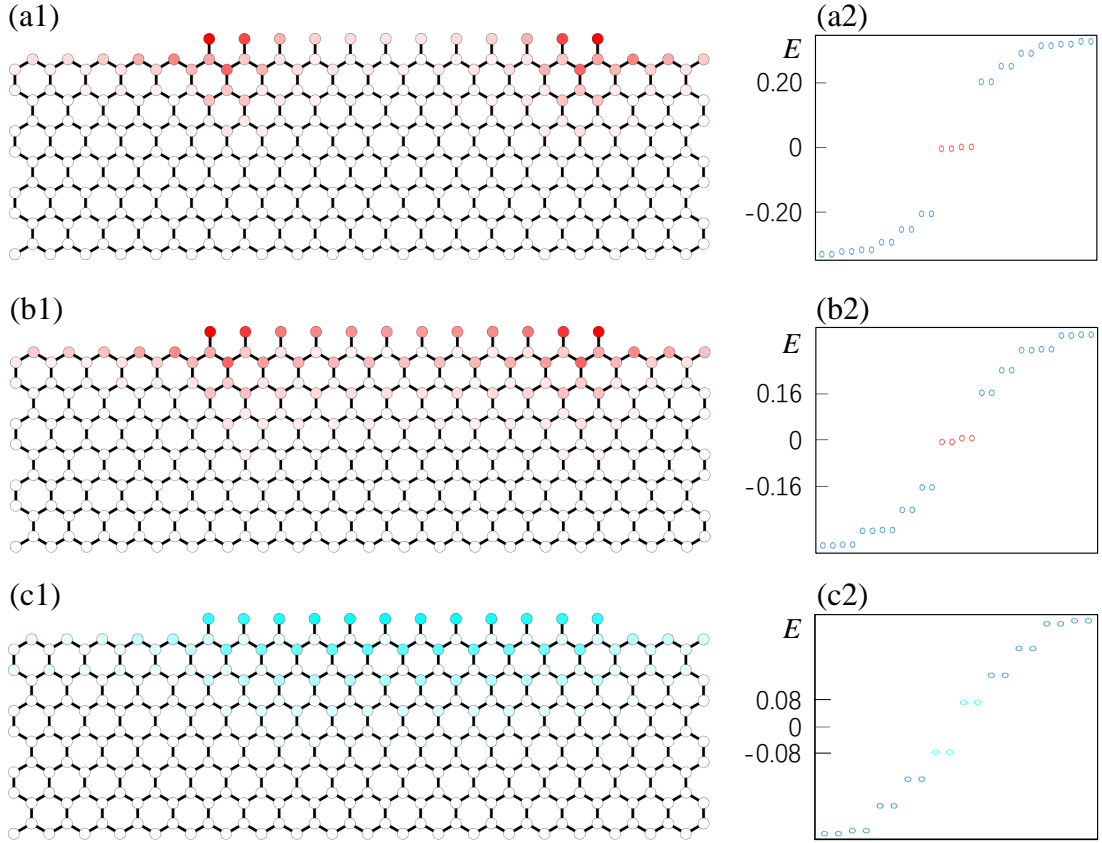


FIG. S4: (Color online) The effect of chemical potential to Majorana Kramers pairs. Chosen parameters are $t = 1$, $\lambda_{so} = 0.1$, $\Delta_0 = \Delta_2 = 0.3$, $\Delta_1 = 0$. In (a1) and (a2), $\mu = 0.1$, the wave functions of Majorana Kramers pairs remain well-localized so their energy splitting (see red dots in (a2)) induced by the overlap of wave functions in the considered finite-size system remains small. In (b1) and (b2), $\mu = 0.2$, the increase of μ reduces the boundary energy gap. As a result, the localization of the wave functions of Majorana Kramers pairs becomes relatively poorer and the energy splitting increases due to the finite size of the geometry. In (c1) and (c2), $\mu = 0.4$, no Majorana Kramers pairs are found as the chemical potential is beyond the critical value. The dots in cyan correspond to the lowest-energy excitations. One can see from (c1) that their wave functions are quite uniform on the beard edge of the upper boundary.

the boundary. For this new topological phase, the Dirac mass of sublattice domain walls will become dominated by Zeeman field on one side and by superconductivity on the other side. Accordingly, one sublattice domain wall will change to host a single Majorana zero mode, instead of a Majorana Kramers pair due to the breaking of time-reversal symmetry.

In Fig.S5, the evolution of boundary energy gap with respect to Zeeman field is shown. One can readily see that the boundary energy gap gets closed and reopened with the increase of B_x , in agreement with the behavior predicted by the low-energy boundary Hamiltonian. In Fig.S6, the numerical results show that each sublattice domain wall hosts one Majorana zero mode when the topological criterion $\min\{B_{b,c}, B_{z,c}\} < B_x < \max\{B_{b,c}, B_{z,c}\}$ is fulfilled. The results indicate that Majorana zero modes at sublattice domain walls can also be achieved in time-reversal symmetry breaking systems. Here it is worth noting that if sublattice-dependent magnetism can be induced on the boundary, the superconductors can be released to conventional s-wave superconductors.

V. TUNING THE POSITIONS OF MAJORANA ZERO MODES BY ELECTRICALLY CONTROLLING THE LOCAL BOUNDARY POTENTIAL

In the main text as well as in Figs.S2 and S6, we have shown that the positions of Majorana zero modes directly follow the change of the positions of sublattice domain walls, indicating that if the terminating sublattices can freely be added or removed, the positions of Majorana zero modes can be manipulated in a site-by-site way. Apparently, this can benefit the detection as well as the implementation of braiding Majorana zero modes. In this section, we show that the positions of Majorana zero modes can also be tuned by electrically controlling the local potential on the boundary, even though the sublattice domain walls are fixed.

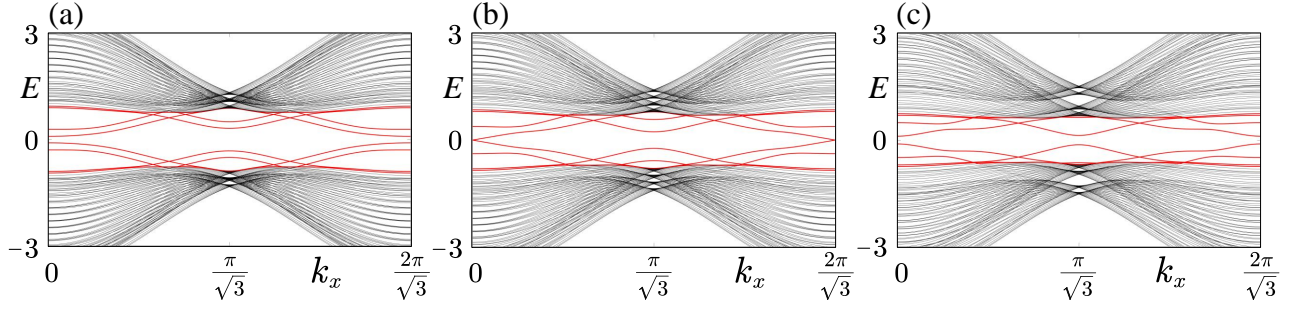


FIG. S5: (Color online) The evolution of boundary energy gap with respect to μ . The lattice geometry is cylindrical with periodic boundary condition in the x direction and open boundary condition in the y direction. The upper y -normal boundary is a beard edge, and the lower y -normal boundary is a zigzag edge. Here the extended s-wave pairing is considered. Chosen parameters are $t = 1$, $\lambda_{so} = 0.1$, $\Delta_0 = 0.2$, $\Delta_2 = 0.3$, $\Delta_1 = 0$. (a) $B_x = 0.1$, the mid-gap red lines show the existence of a finite gap in the boundary energy spectrum. (b) $B_x = 0.191$, the boundary energy gap vanishes, corresponding to the critical point of a boundary topological phase transition. (c) $B_x = 0.3$, a gap is reopened in the boundary energy spectrum.

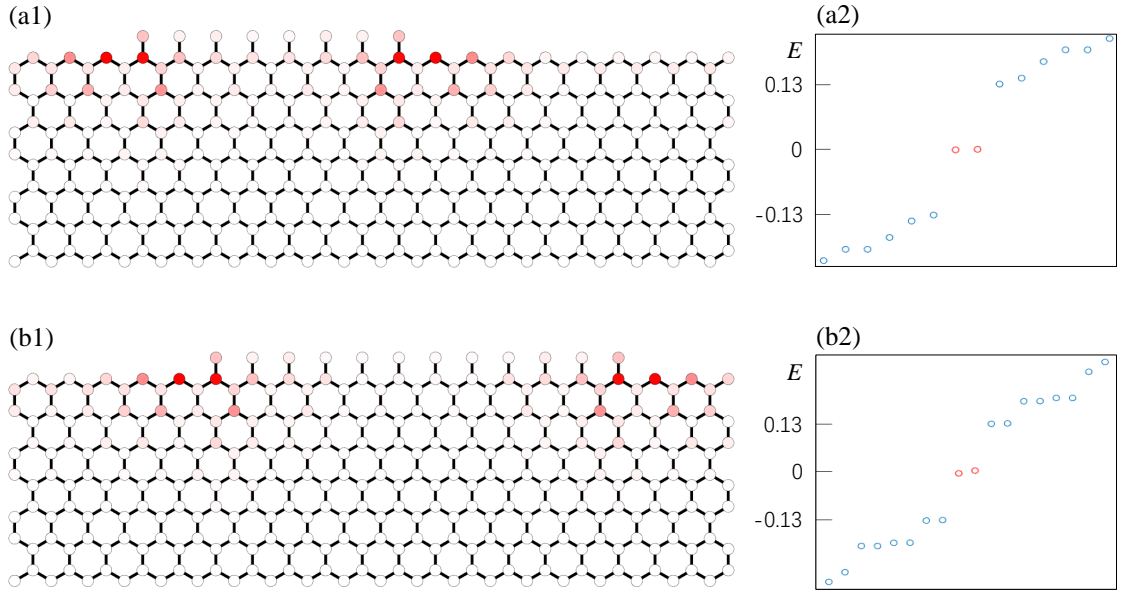


FIG. S6: (Color online) Majorana zero modes at sublattice domain walls. The considered lattice geometry and size are shown explicitly. Here the extended s-wave pairing is considered. Chosen parameters are $t = 1$, $\lambda_{so} = 0.1$, $\mu = 0.1$, $\Delta_0 = 0.2$, $\Delta_2 = 0.3$, $\Delta_1 = 0$, $B_x = 0.3$. (a1) and (b1) show the distribution of probability density profiles of Majorana zero modes, and (a2) and (b2) show the corresponding energy spectra, respectively. Here we have also only shown the part of eigenvalues closest to zero energy. The middle two dots in red in (a2) and (b2) indicate the existence of two Majorana zero modes. The shade of red color on the lattice sites in (a1) and (b1) reflect that the wave functions of Majorana zero modes are strongly localized around the sublattice domain walls.

To show the tunability, we add a coordinate-dependent on-site potential of the form $\sum_i V_i c_i^\dagger c_i$ to the Hamiltonian, and V_i is chosen to be a nonzero constant only at the neighborhood of the sublattice domain walls. The considered lattice geometry is shown explicitly in Fig.S7. For the convenience of discussion, let us label the lattice sites on the uppermost beard edge from left to right as 1, 2,...,12. In Figs.S7(a1) and (a2), the on-site potential is only added to site 1. From the shade of red color on the lattice sites, it is readily found that the site having the highest weight of the probability density of Majorana zero modes becomes site 2. In Figs.S7(b1) and (b2), the on-site potential is added to sites from 1 to 3. Also from the shade of red color on the lattice sites, it is readily found that the site having the highest weight is now shifted from site 2 to site 4. In Figs.S7(c1) and (c2), the on-site potential is added to sites from 1 to 5. It is readily found that the site having the highest weight changes to site 6. The results demonstrate explicitly that the positions of Majorana zero modes can be manipulated by controlling the local boundary potential.

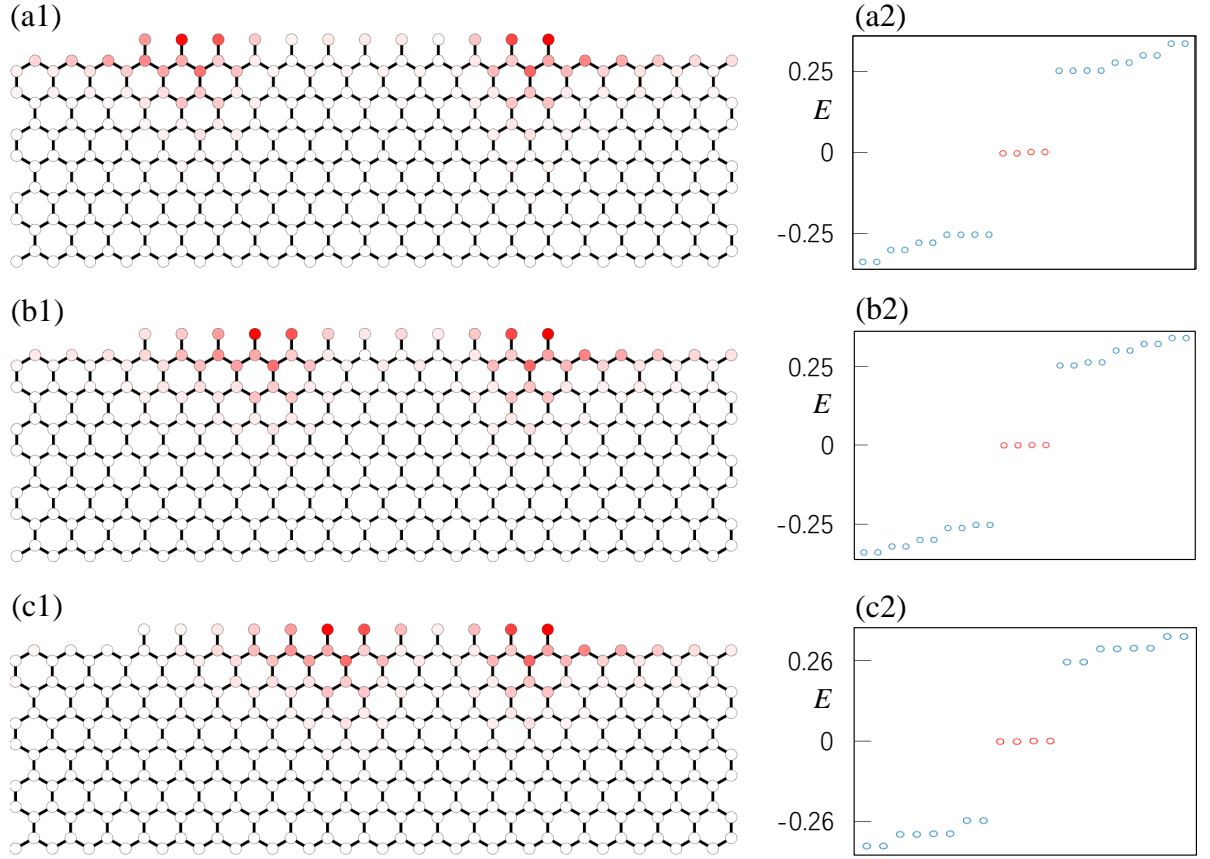


FIG. S7: (Color online) Manipulating the positions of Majorana zero modes by electrically controlling the local potential on the uppermost beard edge. The considered lattice geometry and size are shown explicitly. Here the extended s-wave pairing is considered. Chosen parameters are $t = 1$, $\lambda_{so} = 0.1$, $\mu = 0$, $\Delta_0 = \Delta_2 = 0.3$, $\Delta_1 = 0$, $V = 2$. (a1)-(c1) show the distribution of probability density profiles of Majorana zero modes, with the shade of red color reflecting the weight. (a2)-(c2) are the corresponding energy spectra, also only the part of eigenvalues closest to zero energy are shown. On the uppermost beard edge, the lattice sites from left to right are labeled as 1, 2, ..., 12. In (a1) and (a2), the on-site potential V is only added to the lattice site 1. In (b1) and (b2), the on-site potential V is added to lattice sites from 1 to 3. In (c1) and (c2), the on-site potential V is added to lattice sites from 1 to 5. A comparison of the distributions of wave functions of Majorana zero modes in (a1), (b1) and (c1) clearly show that the positions of Majorana zero modes can be manipulated by controlling the local boundary potential.

VI. SUBLATTICE-SENSITIVE MAJORANA KRAMERS PAIRS IN LIEB LATTICES

In the main text, we have illustrated the essential physics via the honeycomb Kane-Mele model with extended s-wave pairing. In Sec. II, we have shown that sublattice-sensitive Majorana Kramers pairs can also be realized via d-wave and staggered s-wave pairings, reflecting that the physics does not rely on any specific pairing. To further reflect the generality of the physics, in this section we take the Lieb lattice as another example. It is known that the Lieb lattice consists of three sublattices in a unit cell, as shown in Fig.S8. For both x -normal and y -normal edges, it is readily seen that there are two kinds of sublattice terminations. As we will show shortly, the sublattice terminations also have a strong impact on the helical edge states for a topological Lieb insulator, and so sublattice-sensitive Majorana Kramers pairs can also be achieved after introducing appropriate superconductivity to gap out the helical edge states.

For Lieb lattices, first-order topological insulator phases can also be realized by including the next-nearest-neighbor spin-orbit coupling [2],

$$\begin{aligned}
 H = & -t \sum_{\langle ij \rangle, \alpha} c_{i\alpha}^\dagger c_{j\alpha} + i\lambda_{so} \sum_{\langle\langle ij \rangle\rangle, \alpha\beta} (\hat{d}_{ij}^1 \times \hat{d}_{ij}^2) \cdot \boldsymbol{\sigma}_{\alpha\beta} c_{i\alpha}^\dagger c_{j\beta} - \mu \sum_{i\alpha} c_{i\alpha}^\dagger c_{j\alpha} \\
 & + \sum_{\langle ij \rangle} [\Delta_{ij} c_{i,\uparrow}^\dagger c_{j,\downarrow}^\dagger + h.c.].
 \end{aligned} \tag{S68}$$

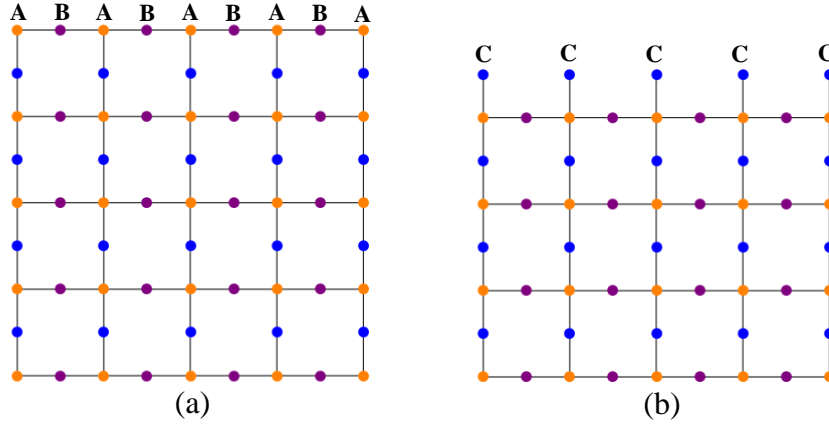


FIG. S8: (Color online) Schematic diagrams of the Lieb lattices. Along both x and y directions, there are two types of sublattice terminations for each edge. For the upper y -normal edge, the sublattice terminations can be $AB\dots AB$ (a) or $C\dots C$ (b).

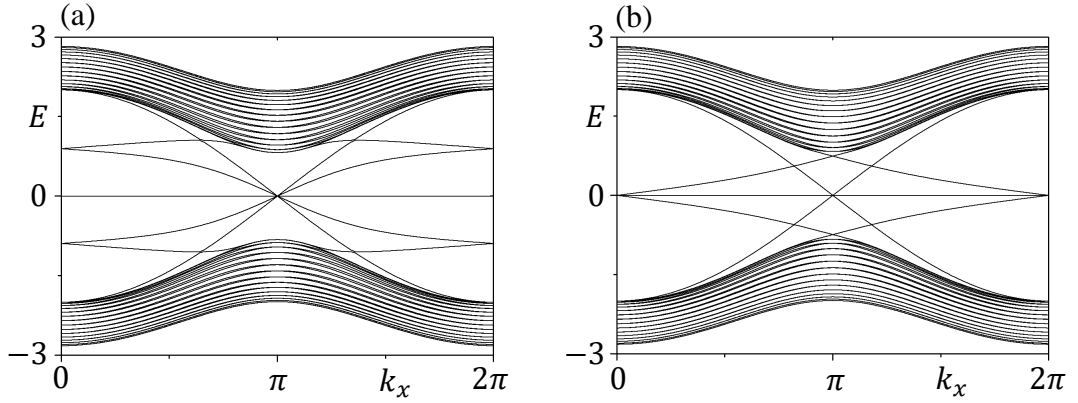


FIG. S9: (Color online) Gapless helical states on the y -normal edges. (a) Both upper and lower edges take the AB -sublattice termination. (b) The lower edge keeps the AB -sublattice termination, and the upper edge is substituted by the C -sublattice termination. Chosen parameters are $t = 1$ and $\lambda_{so} = 0.2$.

Here λ_{so} characterizes the strength of spin-orbit coupling, and \hat{d}_{ij}^1 and \hat{d}_{ij}^2 refers to the two unit bond vectors from site j to its next nearest neighbor i . $\Delta_{ij} = \Delta(\delta_{i\pm\hat{e}_x,j} - \delta_{i\pm\hat{e}_y,j})$ refers to the familiar nearest-neighbor d-wave pairing. In Sec. II, the extension of d-wave pairing has been considered to the next nearest neighbor as the nearest-neighbor pairing fails to gap out the helical edge states in the honeycomb lattice due to crystalline symmetry. As we will show shortly, for Lieb lattices the nearest-neighbor d-wave pairing will gap out the helical edge states and lead to the realization of sublattice-sensitive Majorana Kramers pairs.

In parallel to the study for honeycomb lattice, we also first investigate the sublattice-termination impact on the helical edge states in the normal state. In Fig.S9, we show the energy spectra under two different kinds of sublattice terminations. Fig.S9(a) corresponds to the situation for which both upper and lower edges take the AB -sublattice termination (see Fig.S8(a)). The energy spectrum reveals that the boundary Dirac points for both upper and lower edges are located at the time-reversal invariant momentum $k_x = \pi$. By changing the upper edge's sublattice termination only, the corresponding energy spectrum in Fig.S9(b) shows that the boundary Dirac point on the upper edge immediately shifts from $k_x = \pi$ to $k_x = 0$, reflecting the sensitive dependence of boundary Dirac points on the sublattice termination. Such a sublattice sensitive dependence appearing in both honeycomb and Lieb lattices reflects its generality in lattices with sublattice degrees of freedom.

After considering the nearest-neighbor d-wave pairing and choosing the Fermi level to cross the helical edge-state spectrum, as expected, we find that the helical edge states in the normal state will be gapped and Majorana zero modes can emerge at the sublattice domain walls on the edge, as shown in Fig.S10. The realization of sublattice-sensitive Majorana Kramers pairs in Lieb lattices explicitly demonstrates the generality of the physics.

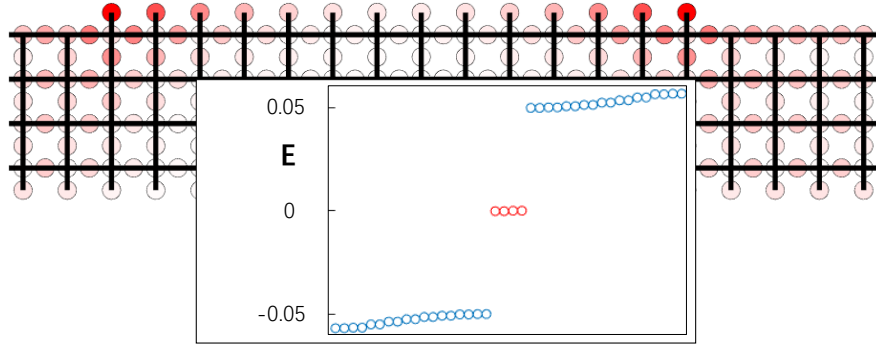


FIG. S10: (Color online) Majorana Kramers pairs at sublattice domain walls on the upper y-normal edge. Periodic boundary condition is imposed in the x direction. Chosen parameters are $t = 1$, $\lambda_{so} = 0.2$, $\mu = -0.2$, $\Delta = 0.3$. The energy-spectrum inset shows the existence of two pairs of Majorana Kramers pairs (four red dots). The probability density files show that the two pairs of Majorana Kramers pairs are sharply localized around the sublattice domain walls.

* These authors contributed equally to this work.

† Electronic address: yanzhb5@mail.sysu.edu.cn

[S1] A. Haim, E. Berg, K. Flensberg, and Y. Oreg, Phys. Rev. B **94**, 161110 (2016), URL <https://link.aps.org/doi/10.1103/PhysRevB.94.161110>.

[S2] C. Weeks and M. Franz, Phys. Rev. B **82**, 085310 (2010), URL <https://link.aps.org/doi/10.1103/PhysRevB.82.085310>.